



## Synthesis and Characterization of Cellulose Microcrystals–Chromium Oxide Nanocomposites: Enhancing Surface, Thermal, and Optical Properties



CrossMark

Sara A. Abdelmoniem <sup>a</sup>, Abeer A. Faheim <sup>a</sup>, Mona T. Al-Shemy <sup>b\*</sup>, and  
Zeinab H. Abd El –Wahab <sup>a</sup>

<sup>a</sup> Chemistry Department, Faculty of Science (Girl's), Al-Azhar University, Youssif Abbas St., Nasr-City, Cairo, Egypt, P.O. Box 11754.

<sup>b</sup> Cellulose and Paper Department, National Research Centre, 33 El-Bohouth St. (Former El-Tahrir St), Dokki, Giza, Egypt.

\* Corresponding author: Mona T. Al-Shemy. E-mail: [mt.el-shemy@nrc.sci.eg](mailto:mt.el-shemy@nrc.sci.eg). Tel: +2-01154456633. El Buhouth St., Dokki, Cairo, Egypt Postal Code 12622. Orcid ID: 0000-0001-9290-5955.

### Abstract

This study developed a novel nanocomposite with expected potentially broad applications in different fields by synthesizing biopolymers cellulose microcrystal@chromium oxide (CMC@Cr<sub>2</sub>O<sub>3</sub>) and activated cellulose microcrystal@chromium oxide (ACMC@Cr<sub>2</sub>O<sub>3</sub>) nanocomposites using an environmentally friendly facile sonication method. The effects of activation of CMC on the characteristics of synthesized Cr<sub>2</sub>O<sub>3</sub> nanocomposite were also examined in the study. The creation of CMC@Cr<sub>2</sub>O<sub>3</sub>, and ACMC@Cr<sub>2</sub>O<sub>3</sub> were investigated employing FTIR, DRS-UV-Vis, SEM, EDX, mapping, XRD, VSM, and TGA techniques. These studies illuminated the optical properties, particle size distribution, crystallinity, and thermal stability and the results demonstrated higher thermal stability, paramagnetic properties, and semiconductor nature properties. Also, surface enhancing was observed upon monitoring some structural parameters extracted from powder x ray diffraction study. The magnetic hysteresis analysis revealed paramagnetic behavior in CMC@Cr<sub>2</sub>O<sub>3</sub> and ACMC@Cr<sub>2</sub>O<sub>3</sub>, as neither exhibited magnetic saturation at the maximum field. Further examination indicated that the activation process significantly influenced the magnetic properties, with ACMC@Cr<sub>2</sub>O<sub>3</sub> displaying lower saturation magnetization (Ms), reduced remanent magnetization (Mr), and lower coercivity (Hci) compared to the non-activated CMC@Cr<sub>2</sub>O<sub>3</sub> sample. These variations are attributed to the activation process altering the ionic environment, chain conformation, and structural network of the polymer matrix, resulting in diminished magnetic responses. Moreover, changes in nucleation and growth processes of Cr<sub>2</sub>O<sub>3</sub>, as evidenced by SEM and mapping analyses, alongside the activation-induced modifications in the polymer matrix, appeared to hinder the formation of larger or more optimally aligned magnetic domains. Structural enhancements, as inferred from powder X-ray diffraction data, were also observed, supporting these findings.

Keywords: Cellulose microcrystal (CMC); Chromium oxide nano-biocomposite; Green synthesis; XRD; SEM; VSM.

### 1. Introduction

One of the most significant organic substances created in the biosphere is cellulose, an omnipresent renewable natural biopolymer on Earth. Many different kinds of organisms, including bacteria, marine creatures, and plants at all levels of development, biosynthesize it [1]. Wood and plant fibers, including cellulose, have many practical applications, including energy production, construction, papermaking, textiles, and apparel. Evidenced by the vast array of enterprises dealing with forest products, paper, textiles, etc., the utilization of natural cellulose-based materials persists to this day [2–4]. Several varieties of cellulose exist, each with a unique microstructure and set of distinguishing features identified by the fibers' length and diameter. Cellulose microcrystals (CMC) are among the most frequently extracted and employed materials across various industrial sectors [5–7]. The unique properties and characteristics of CMC fibers, such as their biocompatibility, low density, large surface area, renewability, high mechanical properties, biodegradability, and non-toxicity, have attracted much attention to their isolation and potential use in composite materials [8].

Research on integrating metallic elements into polymers is currently a highly active field. Several efforts have been undertaken to employ cellulose as a metal clutch using various derivatizations [9–11]. Several of these efforts are founded on incorporating groups that can form chelates, such as carboxylate and amine groups. The interactions between heavy metal ions and cellulose or its derivatives can typically occur through four primary mechanisms:

\*Corresponding author e-mail: [mt.el-shemy@nrc.sci.eg](mailto:mt.el-shemy@nrc.sci.eg); (Mona Tawfik Al-Shemy).

Received date 26 March 2025; Revised date 09 May 2025; Accepted date 18 May 2025

DOI: 10.21608/ejchem.2025.371397.11519

©2025 National Information and Documentation Centre (NIDOC)

- Intercalation within the cellulose matrix.
- Adsorption onto cellulose fibers.
- Formation of chemical bonds with the reactive groups of cellulose.
- Development of complexes with dissolved cellulose degradation products.

Transition metal salts react with cellulose to create coordination bonds with functional groups at cellulose's 6th, 2nd, and 3rd carbon positions. Scientists have been drawn to cellulose-based metal frameworks because of their specialized applications, such as drug delivery systems, water treatment, food and food packaging, antimicrobial agents...etc [12–14]. However, our understanding is limited as scarce information is available on the synthetic methods to create these cellulose-metal frameworks.

By subjecting crystalline cellulose to hydrolysis with diluted acid, it is possible to control the degree of polymerization and create CMC in the micro-size range [15,16]. Typically, the particle size is in the range of 20–80  $\mu\text{m}$ , resembling a material scientist's observation [17]. CMC has found extensive applications in the medicine, food, cosmetics, and light chemical industries due to its low degree of polymerization and large specific surface area. CMC also offers the benefit of being cost-effective [18].

$\text{Cr}_2\text{O}_3$  is a significant technological element due to its multiple applications in catalysts, green pigment, UV-protective coating materials, and visible light transmittance [19]. Due to its high corrosion and wear resistance, low coefficient of friction, and outstanding optical and adiabatic properties,  $\text{Cr}_2\text{O}_3$ —the hardest oxide—is also the most desired. It also has a high melting point of 2435  $^\circ\text{C}$  and is resistant to oxidation at high temperatures [20,21]. There has been a surge of interest in developing nano- $\text{Cr}_2\text{O}_3$  with exceptional catalytic properties, cost-effectiveness, and energy efficiency [22]. It has been utilized in various applications such as photocatalysis, antimicrobial properties, and gas sensitivity [23–26].

Although extensive research exists on preparing various metal and metal oxides [17,27–32], studies on synthesizing  $\text{Cr}_2\text{O}_3$  using CMC as an organic template remain limited. This study introduces an innovative method that dopes  $\text{Cr}_2\text{O}_3$  into CMC, significantly enhancing its physical, chemical, and thermal properties. Using an environmentally friendly method, CMC can be made more robust and resistant to wear, has better thermal stability, improved optical properties [such as increased absorbance and altered optical energy gap], and electrical conductivity (e.g., suitable for use in electronic devices). Moreover, the influence of alkali surface modification on CMC was examined to assess its effect on the physical and chemical properties of the synthesized  $\text{CMC@Cr}_2\text{O}_3$  composite. A comprehensive analysis of the produced composites was conducted utilizing FTIR, SEM, EDS mapping, TGA, XRD, DRS, and VSM techniques.

## 2. Experimental

### 2.1. Materials

*Vicia faba* hulls were collected from a local mill. After thorough washing and rubbing with water to remove dirt, they were dried in an oven set at 50  $^\circ\text{C}$  for 72 hours. Subsequently, the dried hulls were ground to a 0.5-micron mesh size in preparation for further examination and processing. The chemical composition analysis of *Vicia faba* hulls was conducted as follows:  $\alpha$ -cellulose content was determined to be  $51.23 \pm 1.05\%$  using the Tappi T 203 cm-99 method; hemicellulose content was  $26.53 \pm 0.21\%$ , calculated as the difference between holocellulose and  $\alpha$ -cellulose; lignin content was  $10.66 \pm 0.08\%$ , measured following the Tappi T 222 om-02 protocol; ash content was  $3.35 \pm 0.03\%$ , determined via the Tappi T 211 om-02 method; and extractives content was  $0.31 \pm 0.01\%$ , assessed using Tappi T 204 cm-07. These results demonstrate cellulose as the predominant structural component in the hulls, alongside significant contributions from hemicellulose and lignin. Sodium hydroxide (99 %) was obtained from Laboratory Rasayan (SD Fine Chem, Mumbai, India), Chromium chloride hexahydrate [ $\text{CrCl}_3 \cdot 6\text{H}_2\text{O}$ ], was purchased from Sigma-Aldrich. The other reagents were analytical grade and did not require any additional purification before use.

### 2.2. Preparation of materials under investigation

#### 2.2.1. Production of Cellulose microcrystals (CMC)

CMC were extracted from fine *Vicia faba* hulls as were reported previously with slight modification [33]. In brief, three subsequent processing treatments were followed: (1) pulping with 0.4N NaOH at 140  $^\circ\text{C}$  for 1.5 h, (2) delignification using the conventional three-stage method of the sodium chlorite bleaching process, (3) acid hydrolysis treatment with 2N  $\text{H}_2\text{SO}_4$  under reflux for  $\frac{1}{2}$  hour. Each processing step was followed by adequate washing with tap water before being squeezed and left wet without drying till the next step. The overall yield of the processed material, calculated based on the raw *Vicia faba* hulls, was 40%. This yield reflects the efficiency

of the extraction and purification methods applied while processing the hulls into their constituent component of  $\alpha$ -cellulose to CMC.

### 2.2.2. Activation of cellulose microcrystals (ACMC)

As opposed to those in the crystalline parts of the biopolymer, which could result in an inhomogeneous reaction at the molecular level, the hydroxyl groups on the surface of the fibres or in the amorphous regions of the material are more accessible to the reagent. As a result, cellulose typically goes through a pretreatment or activation phase before being subjected to a chemical reaction. This approach is used both in the workplace and in the lab [34]. For activation of cellulose microcrystals (ACMC), 50 g of CMC, as obtained earlier, was suspended in 200 ml of distilled water, and then 2.5 g of NaOH was added. The mixture was continuously stirred for two hours at a controlled temperature of 30 °C to ensure uniform interaction among the components. The resulting cellulosic materials were carefully filtered using filter paper to separate them from the reaction medium. To achieve purity and neutrality, the materials were thoroughly washed with distilled water until no residual acidity or alkalinity remained. The prepared samples were oven-dried at 40 °C for 48 hours.

### 2.2.3. Fabrication of CMC@Cr<sub>2</sub>O<sub>3</sub> and ACMC@Cr<sub>2</sub>O<sub>3</sub>

A dry weight of 1.6214 g (0.01M) of CMC or 2.2808 of ACMC was mixed with 2.6645 g (0.01M) of CrCl<sub>3</sub>.6H<sub>2</sub>O dissolved in 100 mL of methanol - distilled water solution. Following this, the mixtures were sonicated in an ultrasonic water bath for two hours at 50 °C. The deep green CMC@Cr<sub>2</sub>O<sub>3</sub> and ACMC@Cr<sub>2</sub>O<sub>3</sub> precipitates were filtered through filter papers and dried for 24 hours at 30 °C.

## 2.3. Characterizations

- The optical characteristics of the prepared CMC, ACMC, CMC@Cr<sub>2</sub>O<sub>3</sub> and ACMC@Cr<sub>2</sub>O<sub>3</sub> were investigated using DRS Spectrophotometer - Jasco V-570, Spectral range from 190 nm to 2500 nm.
- The FT-IR spectra of the variously produced samples were recorded on a JASCO FT-IR 6100 spectrometer (Tokyo, Japan). A resolution of 4 cm<sup>-1</sup> and 64 scans were used to conduct the measurements within the 400-4000 cm<sup>-1</sup> range.
- A Malvern Panalytical Empyrean X-ray diffractometer from the Netherlands was used to investigate the XRD patterns of the materials in their as-prepared state. The instrument has an incident monochromatic X-ray angle ranging from 5° to 80° .
- An electron scanning electron microscope, specifically a Quanta FEG-250 from Waltham, MA, USA, operating at a voltage of 20 kV, was employed to visualize and analyze components in dry samples using energy-dispersive X-ray spectroscopy (EDAX).
- A differential scanning calorimeter (SDTQ600 V20.9 Build 20) was used to study thermogravimetric and derivative thermogravimetric studies (TGA and DTG, respectively). Measurements were made in an inert nitrogen atmosphere within a temperature range of 25 to 750 °C. The testing rate was 10 °C/minute.
- All magnetic measurements were conducted at room temperature using a vibrating sample magnetometer (VSM) from Lake Shore, USA (model VSM-7410) with a maximum applied field of 20 kG.

## 3. Results & Discussion

### 3.1. Comparative study of the extracted CMC

Some specific properties of the extracted CMC from *Vicia faba* hulls were established through the studied different techniques and were listed in Table 1. These specific properties are further compared with that of CMC isolated from a variety of sources in addition to the commercial one [35–39]. Table 1 displays the cellulose content, ash content, crystalline properties, and thermal resistance of CMC extracted from *Vicia faba* hulls in comparison with that of other sources, and commercial CMCs. It is clear from the table that the crystallinity index of CMC in the present work was promising than all of the CMCs reported. In fact, the present work confirms the importance of cellulose extraction from *Vicia faba* hulls and could be substituted instead CMC-commercial in variable applications.

Table 1: Comparison of CMC extracted from *Vicia faba* hulls with different sources

Sources	Parameters under study						References
	Yield (%)	Cellulose content (%)	Ash (%)	Crystallinity Index (%)	Crystallite size (nm)	Thermal resistance (°C)	
<i>Vicia faba</i> hulls	40.00	51.23	3.35	82.50	22.97	225	Present study
<i>Tamarindus indica</i> seeds	44.15	90.57	0.92	77.60	---	230	[39]
<i>Borassus flabellifer</i> flower	59.00	73.20	0.40	69.81	70.73	320	[38]
<i>Citrus x sinensis</i>	67.82	70.00	---	72.54	9.63	308	[37]
<i>S. spontaneum</i>	83.00	83.33	0.72	74.06	---	338	[36]
<i>Myriophyllum verticillatum</i>	45.43	65.72	---	68.84	---	317.32	[35]
CMC- commercial	---	98.59	0.05	74-80.60		220-300	[39]

### 3.2. Infrared spectroscopy

FT-IR analysis was used to investigate the chemical configurations of the functional groups in every sample. The FT-IR spectra clearly show the absorption trends of the samples at several frequency (wavenumber) ranges [40]. Table 2 provides a detailed summary of the fabricated samples' FTIR spectral band allocations. It is evident from Fig. 1 and Table 2 that the wavenumber and intensity of the characteristic bands shift when NaOH activates CMC. As a result, a blue shift of peak frequencies occurs as their intensities decrease. Conversely, CMC@Cr<sub>2</sub>O<sub>3</sub> and APMC@Cr<sub>2</sub>O<sub>3</sub>, a shift in intensity and frequency occurs, and new bands also form.

For example, the peak at 3416 and 3417 cm<sup>-1</sup> in CMC and APMC, respectively, corresponding to the stretching vibration of the -OH intramolecular hydrogen bonds went to a lower frequency when decorated with Cr<sub>2</sub>O<sub>3</sub>. Moreover, the appearance of a Cr-O vibration peak at 561 and 560 cm<sup>-1</sup> confirms that Cr<sub>2</sub>O<sub>3</sub> has been deposited on the surface of CMC and APMC, respectively [41]. The differences in peak positions and intensities between the compounds CMC@Cr<sub>2</sub>O<sub>3</sub> and APMC@Cr<sub>2</sub>O<sub>3</sub> indicate the variations in how the Cr metal is bonded to each nanocomposite. The Cr-O bond is typically observed in the 550 to 650 cm<sup>-1</sup> range of the FTIR spectrum [42]. However, in this study, the range can vary slightly depending on the compound and its environment.

Table 2: Main FT-IR spectral vibrations (cm<sup>-1</sup>) for the prepared samples

Band assignment	Band position (cm <sup>-1</sup> )				References
	CMC	APMC	CMC@Cr <sub>2</sub> O <sub>3</sub>	APMC@Cr <sub>2</sub> O <sub>3</sub>	
-OH stretching intramolecular hydrogen bonds.	3416	3417	3398	3403	[43]
CH stretching, CH <sub>2</sub> asymmetric stretching.	2899	2913	2902	2914	[44]
OH of water absorbed from cellulose.	1641	1636	1643	1644	[45]
C-H in plane deformation.	1442	1444	1431	1430	[46]
CH symmetric bending methoxyle group, CH deformation vibration or CH <sub>2</sub> vibration.	1371	1372	1371	1371	[47]
CH <sub>2</sub> wagging.	1162	1162	1163	1163	[47]
Ring asymmetric stretching, C-C & C-O stretching.	1114	1114	1116	1115	[48]
C-O stretching.	1057	1057	1058	1058	[48]
C-H out of plane in position in ring stretching in cellulose due to β-linkage.	895	898	998	897	[49,50]
ν M-O.	--	--	561	610	[42]

Table 3: XRD data of 2-theta, *d*-space, FWHN, particle size (*D*), micro strain ( $\epsilon$ ), stacking fault (SF), dislocation density ( $\delta$ ), and crystallinity index (*CrI*)

Compound	Angle (2θ°)	<i>d</i> (Å)	FWHM (°)	<i>D</i> (nm)	$\epsilon$	SF	$\delta$ (nm <sup>-2</sup> )	<i>CrI</i> (%)
CMC	22.78	3.90	1.32	22.97	28.13X10 <sup>-3</sup>	11.38X10 <sup>-3</sup>	1.93X10 <sup>-3</sup>	82.50
APMC	22.61	3.93	1.57	33.77	49.83X10 <sup>-3</sup>	14.91 X10 <sup>-3</sup>	1.97X10 <sup>-3</sup>	79.40
CMC@Cr <sub>2</sub> O <sub>3</sub>	22.46	3.96	0.80	26.74	15.72X10 <sup>-3</sup>	6.46 X10 <sup>-3</sup>	1.98X10 <sup>-3</sup>	60.29
APMC@Cr <sub>2</sub> O <sub>3</sub>	22.60	3.93	0.81	30.51	13.64X10 <sup>-3</sup>	5.73X10 <sup>-3</sup>	1.96X10 <sup>-3</sup>	76.78

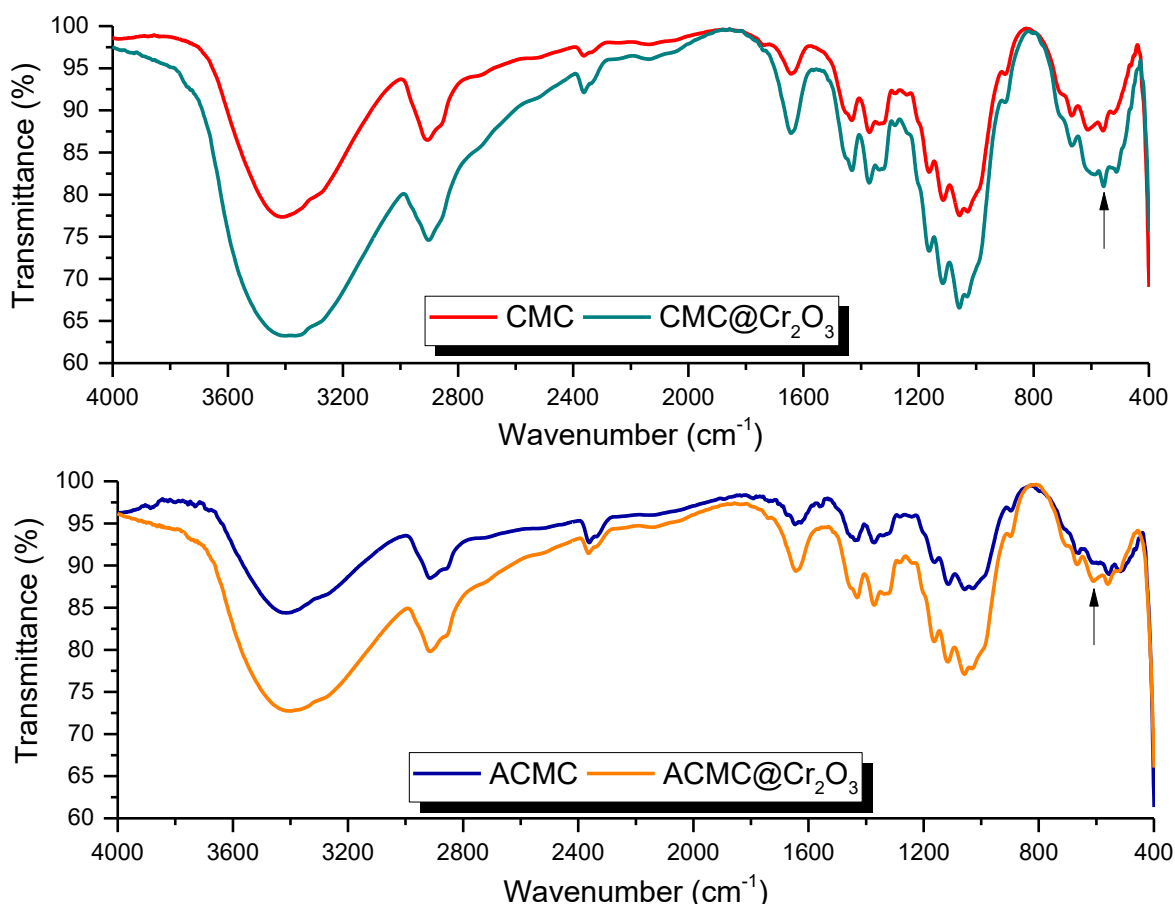


Figure 1: FTIR spectroscopy for fabricated materials under investigation.

### 3.3. X-ray diffraction

An X-ray diffraction examination was conducted to analyze the structure and get the diffractograms of various cellulose and CMC samples and their corresponding  $\text{Cr}_2\text{O}_3$  frameworks. Following Segal's equation [51], the crystalline indices of CMC, ACMC, and their  $\text{Cr}_2\text{O}_3$  framework samples were calculated using various diffractograms.

$$CrI\% = \frac{I_{200} - I_{amp}}{I_{200}} \times 100$$

where  $CrI$  is the crystallinity index,  $I_{200}$  is the maximum intensity of the 200 peak at  $2\theta=22^\circ$  and  $I_{am}$  is the intensity at  $2\theta=18^\circ$ . Figure 2 displays XRD patterns of CMC and ACMC templates, both with and without the presence of  $\text{Cr}_2\text{O}_3$ . CMC and ACMC align closely with CI polymorphism. XRD examination showed no peaks for elemental Cr or crystalline  $\text{Cr}_2\text{O}_3$ , suggesting that the  $\text{Cr}_2\text{O}_3$  is amorphous since amorphous materials lack long-range order, which is why they do not produce distinct peaks in an XRD pattern. This can be related to the fact that in previous studies, crystallized  $\text{Cr}_2\text{O}_3$  was created by annealing the solvothermal product over  $400^\circ\text{C}$ , in contrast to the  $50^\circ\text{C}$  temperature at which the sono-co-precipitation process in this study occurs [52,53].

The size of the crystallites in the samples was determined using the Scherrer formula,  $L(hkl) = 0.9 k / D(hkl)\cos\theta$ , which calculates the size based on the (002) diffraction lines from cellulose [54,55]. The calculated sizes are provided in Table 2. In the presence of  $\text{Cr}_2\text{O}_3$ , the average size of CMC/(CMC@ $\text{Cr}_2\text{O}_3$ ) is 22.97/26.74 nm, unlike the corresponding ACMC (33.77 nm) and ACMC@ $\text{Cr}_2\text{O}_3$  (30.51 nm). This implies that the bonding of CMC or ACMC to  $\text{Cr}_2\text{O}_3$  promotes the transformation of primary cellulose crystallographic structure to a certain degree.

Based on the estimated crystallites size, the dislocation density was calculated in addition to micro strain ( $\epsilon$ ), and stacking fault (SF) as important structural parameters and summarized in Table 3 [56]. The higher value of ( $\delta$ ) for the synthesized CMC@ $\text{Cr}_2\text{O}_3$  than ACMC@ $\text{Cr}_2\text{O}_3$  indicates the presence of imperfections in the crystal structure, furthermore, the significantly higher ( $\epsilon$ ), and (SF) values observed in CMC@ $\text{Cr}_2\text{O}_3$  confirm the presence of more substantial crystal imperfections or structural disorder. This is agreed with the lower value of crystallinity index.

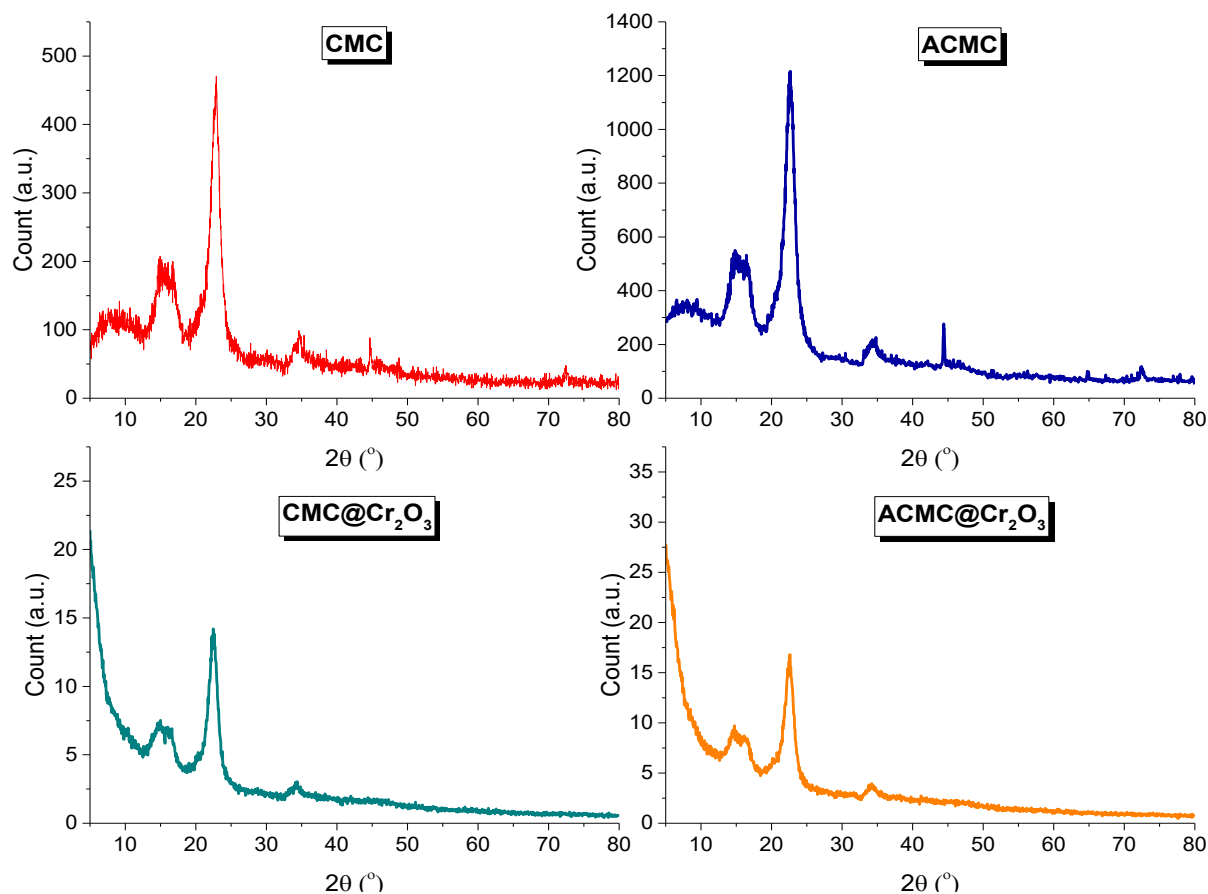


Figure 2: X-ray diffraction patterns for fabricated materials under investigation.

### 3.4. Optical analysis

Figure 3 shows the results of recording the UV-Vis absorbance spectra of neat CMC and ACMC and their respective hybrid  $\text{Cr}_2\text{O}_3$  nanoparticles to evaluate their optical characteristics. Three prominent absorbance peaks are visible in the collected spectra of hybrid  $\text{Cr}_2\text{O}_3$ . Cellulose organic functional groups are linked to the 208 and 246 nm absorbance spectra [57]. It can be seen that the primary cellulose structure in CMC was affected by both the alkali activation and the  $\text{Cr}_2\text{O}_3$  in situ procedures, as these bands shifted to 202; 210 and 258; 246 in the corresponding ACMC and  $\text{CMC@Cr}_2\text{O}_3$ , respectively.

Two sub bands,  $e_g$  and  $t_{2g}$ , form in the Cr  $3d^3$  orbitals as a result of the octahedral field symmetry. The  ${}^4A_{2g} \rightarrow {}^4T_{1g}$  and  ${}^4A_{2g} \leftrightarrow {}^4T_{2g}$  electronic transitions of  $\text{Cr}^{3+}$  ions are represented by the absorbance peaks at 426;430 and 592;592 nm, respectively. Furthermore, at 692 and 736 nm, two faint shoulders can be seen, resulting from the forbidden spin transitions of  ${}^4A_{2g} \rightarrow {}^2T_{1g}$  and  ${}^4A_{2g} \rightarrow {}^2E_g$ , respectively. The bands can be explained by the existence of  $\text{Cr}^{6+}$  ions linked to bulk  $\text{Cr}_2\text{O}_3$  nanoparticles [58].

The Kubelka-Munk function was used to determine the optical band gap ( $E_g$ ) of  $\text{CMC@Cr}_2\text{O}_3$  and  $\text{ACMC@Cr}_2\text{O}_3$ . The claimed standard value is around 3.1 eV, while the absorption spectra of  $\text{CMC@Cr}_2\text{O}_3$  and  $\text{ACMC@Cr}_2\text{O}_3$  at 426 and 430 nm are associated with band gap transitions at about 3.66 and 3.36 eV. Generally, after alkali activating CMC, the band gap of the fabricated  $\text{Cr}_2\text{O}_3$  hybrids drops from 3.66 eV to 3.36 eV. It is possible that vacancies cause impurity levels to build between the prohibited bands, which in turn cause redshift to occur. Redshift is partly caused by holes and oxygen-related defects created by  $\text{Na}^+$  cations in the  $\text{Cr}^{3+}$  lattice site [59,60]. Further, the band-gap energy range (3.66-3.36 eV) of  $\text{CMC@Cr}_2\text{O}_3$  and  $\text{ACMC@Cr}_2\text{O}_3$  is in accordance with the energy gap (2-4 eV) of wide band-gap semiconductors. Therefore, they are considered as worthy contender in lasers, military radars and energy converting systems, and can be employed as efficient semiconductors for developing the new electrical technologies and alternate energy devices [61]

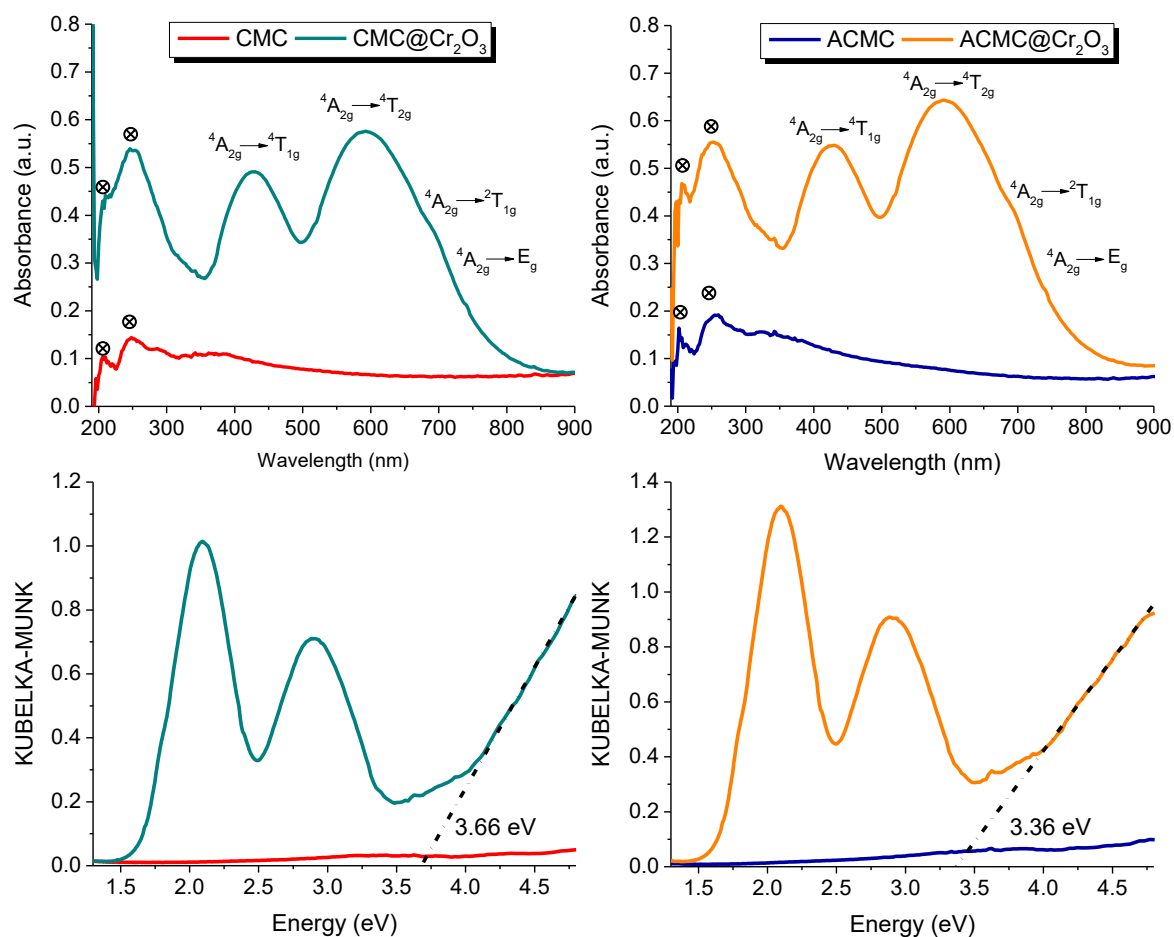


Figure 3: UV-vis DRS spectroscopy for fabricated materials under investigation.

### 3.5. Superficial morphology characteristics of the fabricated samples

The SEM graphs illustrate the morphology of CMC, ACMC, and chromium analog frame samples. Based on the information provided in Figure 4, it is clear that the bleached pulps, when treated with 2N H<sub>2</sub>SO<sub>4</sub>, underwent hydrolysis and formed CMC consisting of small fiber strands that had a rod-like morphology with a length of 100.78  $\mu\text{m}$ . The discovered particles display a distinctive morphology, appearing elongated, cylindrical, and uniformly sized. No differences were observed among the samples after NaOH alkaline activation. The ACMC has an average length of 103.56  $\mu\text{m}$  (Fig. 4). The crystalline fibers have a cylindrical morphology featuring prominent longitudinal striations on one side and a curved configuration with well-defined folds on the opposite side. Conversely, the developed CMC@Cr<sub>2</sub>O<sub>3</sub> and ACMC@Cr<sub>2</sub>O<sub>3</sub> frameworks exhibit comparable CMC particles, except for the Cr coating on the fiber surface. Whereas ACMC@Cr<sub>2</sub>O<sub>3</sub> manifests as crusts covering the fiber surface, CMC@Cr<sub>2</sub>O<sub>3</sub> exhibits distinct Cr<sub>2</sub>O<sub>3</sub> nanoparticles as clusters on the surface of CMC particulates.

Figures 5 and 6 display the results of the composition analysis of the produced samples and their related distribution maps obtained using EDX spectroscopy. The presence of carbon and oxygen peaks can be attributed to the binding energies originating from the pristine CMC [62]. Meanwhile, the ACMC experienced an additional peak due to the binding energy of sodium, providing evidence of the successful activation of CMC. It is important to note that the Na peak persisted in the ACMC@Cr<sub>2</sub>O<sub>3</sub> framework, providing further evidence of effective bonding between Cr and the cellulose matrix through a potential pathway involving partial replacement of Na. The presence of Cr peaks in the EDX spectra of both frameworks, CMC@Cr<sub>2</sub>O<sub>3</sub> and ACMC@Cr<sub>2</sub>O<sub>3</sub>, confirms the effective incorporation of Cr into the CMC and ACMC, respectively. Similarly, the EDX analysis of the produced samples reveals a consistent distribution of all identified components, as shown in Figure 6. The Cr atoms were evenly dispersed throughout the cellulose polymer matrix, together with C and O.

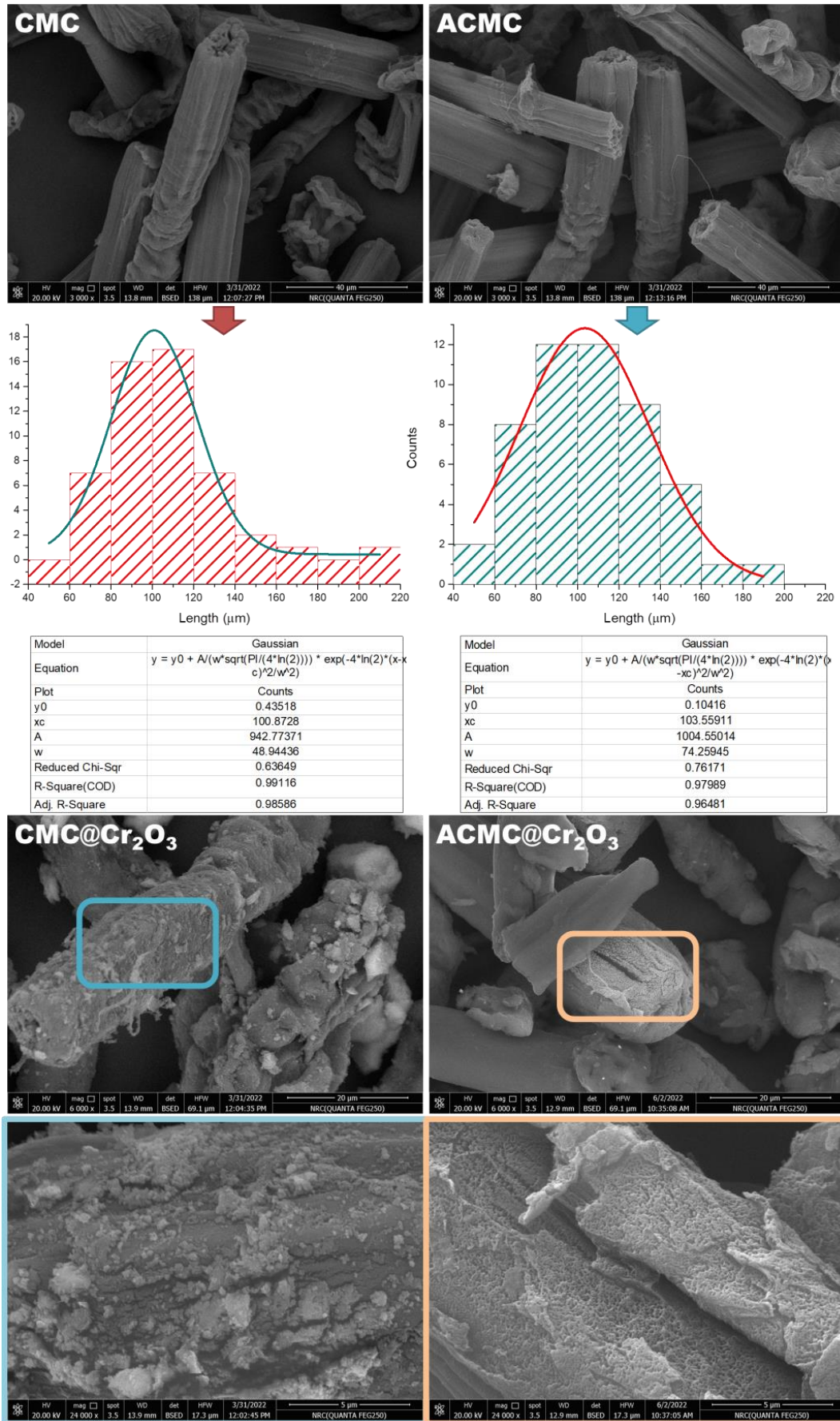


Figure 4: SEM micrographs of fabricated materials under investigation.

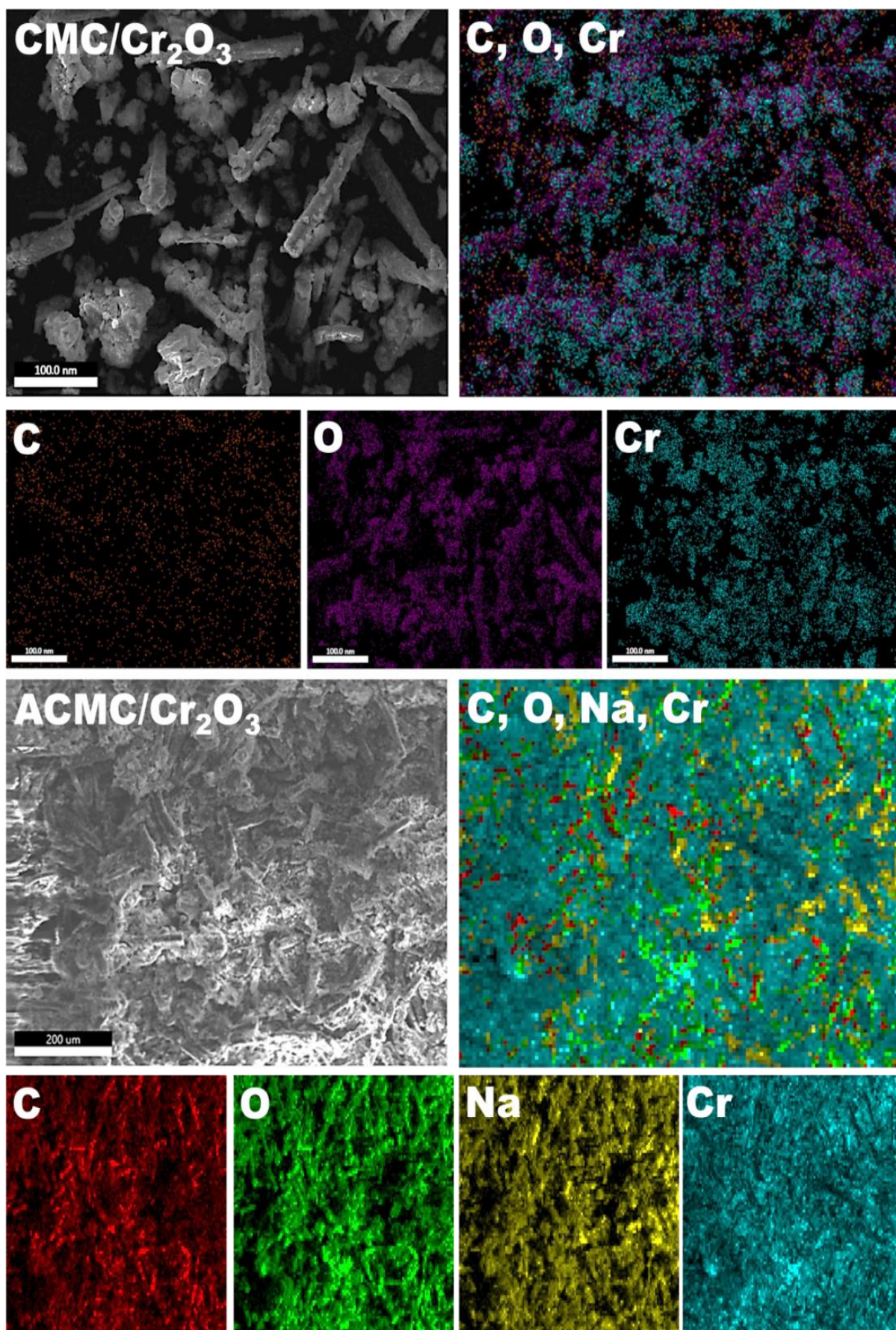


Figure 5: Mapping micrographs of fabricated materials under investigation.

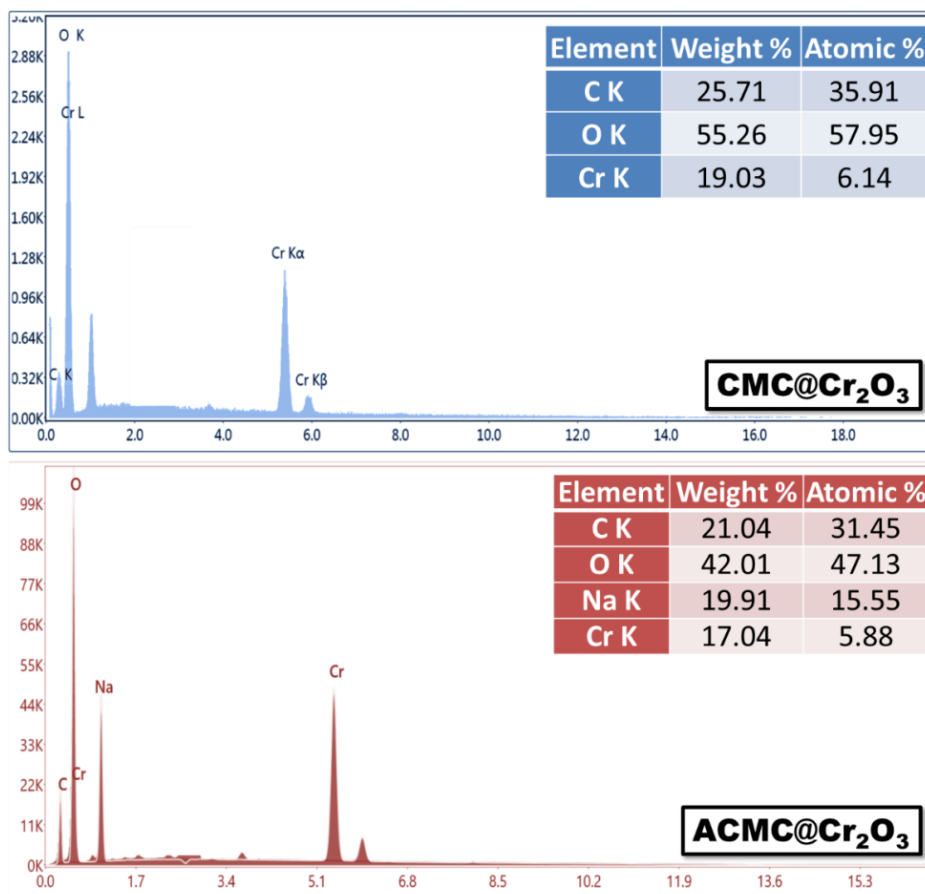


Figure 6: EDAX analysis of fabricated materials under investigation

### 3.6. Thermal analysis

The thermal analysis curves acquired for each phase in the breakdown process were used to identify the typical thermal characteristics for each reaction step. The TGA thermogram obtained for the fabricated CMC and ACMC, along with their respective  $\text{Cr}_2\text{O}_3$ -framework, is presented in Figure 7. Generally, the decomposition curves for CMC and ACMC exhibit a two-step decomposition process, which aligns with previous findings in the literature. Furthermore, it is established that the primary phases consisted of drying at temperatures ranging from 40 to 150 °C, followed by the decomposition of organic substances at temperatures between 225 and 350 °C [63–65].

The dissimilarity in thermal breakdown characteristics and thermal stability between CMC and ACMC becomes evident following alkaline (NaOH) treatment and can be attributed to variations in bonding configuration. The thermogram for CMC and ACMC exhibit two distinct phases of weight reduction occurring between temperatures of 33–377 °C and 33–396 °C, respectively [66]. The initial phase of deterioration takes place within the temperature range of 33–112 and 33–138 °C, resulting in a weight reduction of 1.39% for CMC and 1.87% for ACMC, respectively. In the second stage, the temperature range for CMC was 259–377°C, whereas for ACMC, it was 215–396 °C. The weight loss observed for CMC was 98.73%, but for ACMC, it was 73.03%.

Both  $\text{CMC@Cr}_2\text{O}_3$  and  $\text{ACMC@Cr}_2\text{O}_3$  went through two distinct but related stages of thermal degradation. The loss of water molecules between 44 and 158 °C, and between 35 and 164 °C is the primary cause of the early breakdown stage, which results in a mass loss of 2.74% and 3.35%, for  $\text{CMC@Cr}_2\text{O}_3$  and  $\text{ACMC@Cr}_2\text{O}_3$ , respectively. In the second stage, which takes place between 212 and 365 °C, and between 210 and 365 °C, an estimated 20.29% and 17.52% mass loss, respectively, occurs. So, this lines up with the idea of the pyrolysis of the cellulose analog and the subsequent volatilization of the organic components. When comparing CMC and ACMC, the  $R_{700}$  is 0 and 24.77%, respectively. In the process of creating the char component and impacting the thermal degradation properties of the end product, the bound sodium (Na), in conjunction with ACMC, safeguards the bulk structure of the cellulose fibers. Therefore, the complete breakdown of cellulose and the evolution of organic components occurred during the thermal decomposition stage above CMC decomposition temperature, thereby ending the ACMC thermal decomposition process. After thermal degradation of  $\text{CMC@Cr}_2\text{O}_3$  and  $\text{ACMC@Cr}_2\text{O}_3$ , respectively, the residual weight at 700°C is 65.61% and 72.34%, which represents the fraction of remaining  $\text{Cr}_2\text{O}_3$  safeguarding the bulk structure of cellulose fiber.

At room temperature, the hybrid  $\text{Cr}_2\text{O}_3$  structures under investigation remain stable, but as their temperature increases, they slowly break down. Dehydration and pyrolytic degradation are the two main steps in the thermal breakdown of these frameworks. The successive removal of hydrated water molecules is involved in the dehydration processes of  $\text{CMC}@Cr_2O_3$  and  $\text{ACMC}@Cr_2O_3$ . Following, the cellulose breaks down as a result of the organic molecules pyrolytic disintegration. Thermal breakdown produces the organic metallic hybrid residue as the final product in the  $\text{CMC}@Cr_2O_3$  and  $\text{ACMC}@Cr_2O_3$  frameworks, which involve only one phase of cellulose partial loss.

For the second primary degradation stage in the decay process of the examined materials, Table 4 provides the data for the thermal and kinetic parameters obtained from the TG and DTG curves. The decay behaviors of the key components of the materials being examined, notably cellulose, characterize the temperature range known as the active pyrolysis zone, which is of particular interest. In this regard, cellulose is the principal component that gives rise to volatile components. To determine the thermodynamic and kinetic parameters for the main stage of decomposition, one can apply Coats and Redfern's theory in conjunction with TG analyses and pseudo-first-order kinetics (Fig. 8). The variables listed in Table 4 include activation energies ( $E_a$ ), pre-exponential factors ( $A$ ), entropy ( $\Delta S_a$ ), Gibbs free energy ( $\Delta G_a$ ), and enthalpy ( $\Delta H_a$ ) of activation [67].

In comparison to their parent CMC and ACMC,  $\text{CMC}@Cr_2O_3$  and  $\text{ACMC}@Cr_2O_3$  exhibited reduced levels of  $E_a$  and  $A$ . The presence of the  $\text{Cr}_2\text{O}_3$  fragment on the cellulose fibers may explain why small amounts of energy are needed to initiate the pyrolysis processes. Thus, the activation energy is reduced due to an alteration in the pyrolysis reaction pathway caused by  $\text{Cr}_2\text{O}_3$  coating the cellulose fibers in CMC and ACMC.  $\text{Cr}_2\text{O}_3$  nanoparticles, as an inorganic and non-combustible barrier, can serve a dual purpose in the thermal stability of CMC and ACMC composite. They can prevent the CMC and ACMC from being physically combustible by isolating them from oxygen and heat. In addition, they have the potential to lessen combustion by altering the chemical breakdown route, which could lead to the stabilization of intermediates or the inhibition of the production of combustible and volatile byproducts. Consequently, this combined effect is responsible for the composite's thermal stability and the observed drop in activation energy. The same was observed in preceding studies, where more thermally stable materials revealed lower activation energy [44,68]. Furthermore, the spontaneity of this process is usually measured by the difference in  $\Delta G_a$  between the energies of the reactant and the activated states. As a result, the heat degradation of  $\text{CMC}@Cr_2O_3$ ,  $\text{ACMC}@Cr_2O_3$ , neat CMC, and ACMC, as  $\Delta G_a$  has (+) values, cannot be regarded as a spontaneous process. Commonly, the values of  $\Delta S_a$  and  $\Delta H_a$  for thermal processes are (-) and (+), respectively. The rise in temperature leads to accelerated degradation, as the  $\Delta H_a$  values suggest an endothermic condition between the activated complex and the reactant. In contrast to neat CMC and ACMC, where the  $\Delta S_a$  (+) values indicate more structural freedom, the transition state of  $\text{CMC}@Cr_2O_3$  and  $\text{ACMC}@Cr_2O_3$  exhibited less structural freedom, as reflected by the  $\Delta S_a$  (-) values [69,70]. The data reported above clearly demonstrated that the thermal stability of the neat CMC and ACMC was enhanced by  $\text{Cr}_2\text{O}_3$  covering. Also, like the thermal stability of CMC was increased by alkali activation with NaOH,  $\text{ACMC}@Cr_2O_3$  displays thermal improvements than  $\text{CMC}@Cr_2O_3$ .

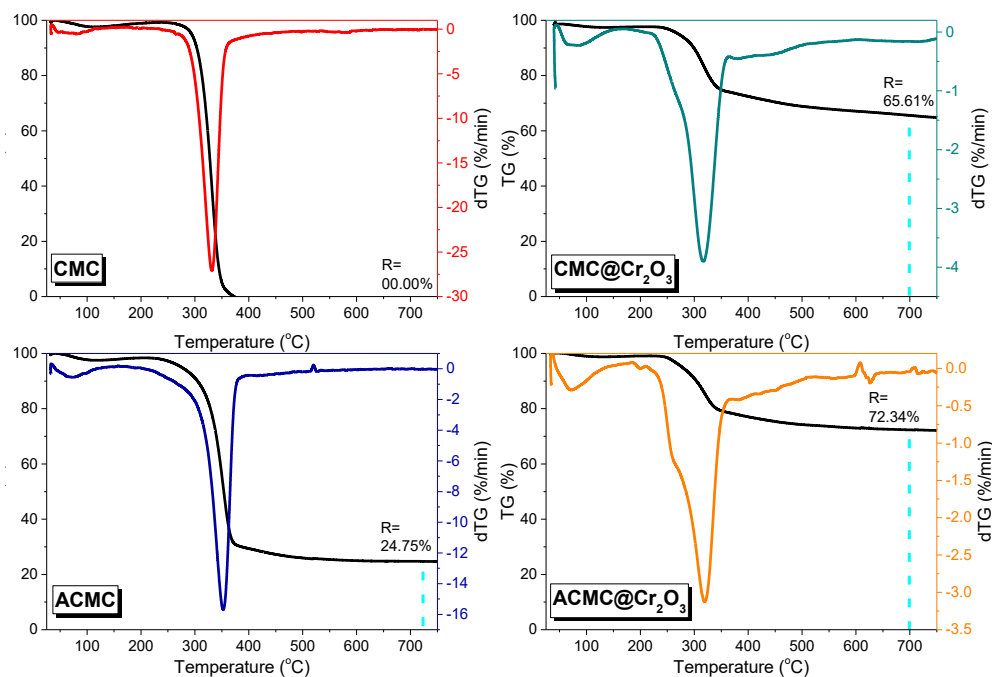


Figure 7: TG and DTG analysis of fabricated materials under investigation.

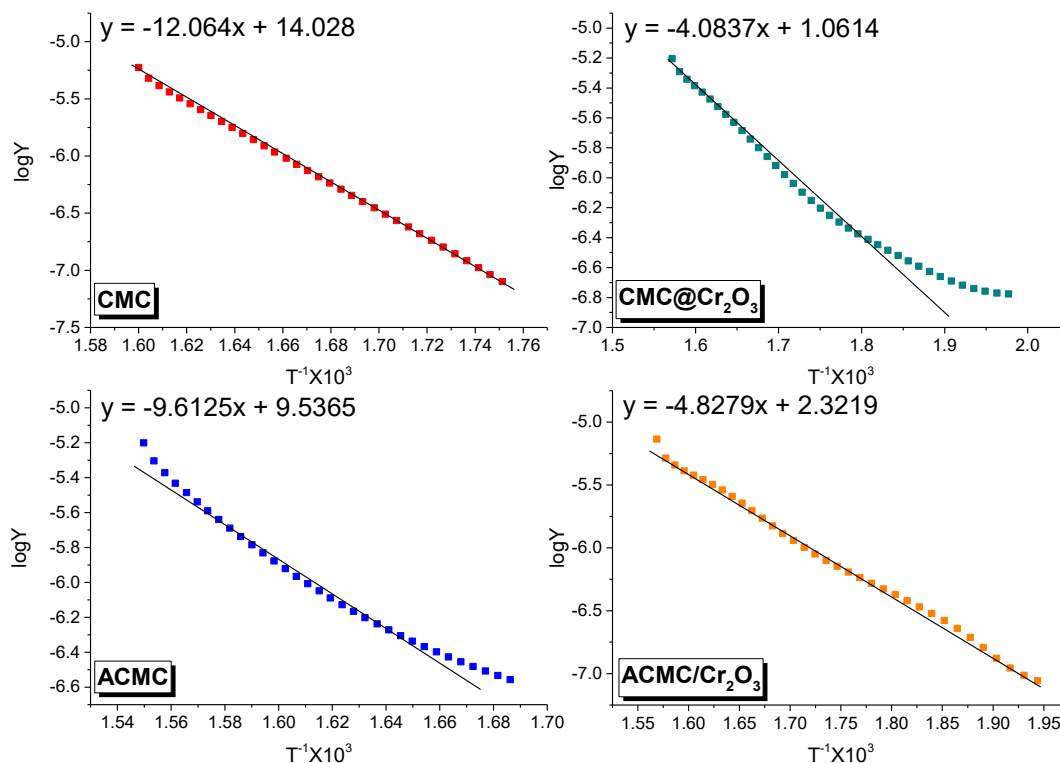


Figure 8: Coats-Redfern plots for the main degradation step of fabricated materials, whereas  $\text{Log } Y = \log \left[ \log \left( \frac{w_f / (w_f - w)}{T^2} \right) \right]$

### 3.7. Magnetic hysteresis analysis

At room temperature, a vibrating sample magnetometer (VSM) with an applied field of  $\pm 20$  kG is utilized to evaluate the magnetic properties of  $\text{CMC}@Cr_2O_3$  and  $\text{ACMC}@Cr_2O_3$ . Variation of magnetization ( $\mu$  emu/g) with applied magnetic field (G) at room temperature is shown in Fig.9. As can be observed,  $\text{CMC}@Cr_2O_3$  and  $\text{ACMC}@Cr_2O_3$  shows a paramagnetic phase that is not magnetically saturated even at 20 kG applied field [71]. Additionally, some parameters can be extracted from the hysteresis loops were listed in Table 5. It is observed that,  $\text{ACMC}@Cr_2O_3$  displays lower saturation magnetization ( $M_s$ ), reduced remanent magnetization ( $M_r$ ), and coercivity ( $H_{ci}$ ) compared to the  $\text{CMC}@Cr_2O_3$  sample. Activation process of CMC offers significant insights into the variations in magnetic properties compared to inactivated matrix. Activation process can change ionic environment, chain conformation, and the network's structure result in a diminished overall magnetic response. Accordingly, particle size and dispersion may vary due to changes to the nucleation and growth processes of  $Cr_2O_3$  (see Figs. 4 & 5). Furthermore, the activation process induced modifications in the polymer matrix hinder the formation of larger or more optimally aligned domains, which would explain why the magnetic properties reveal the interaction between the magnetic domains.

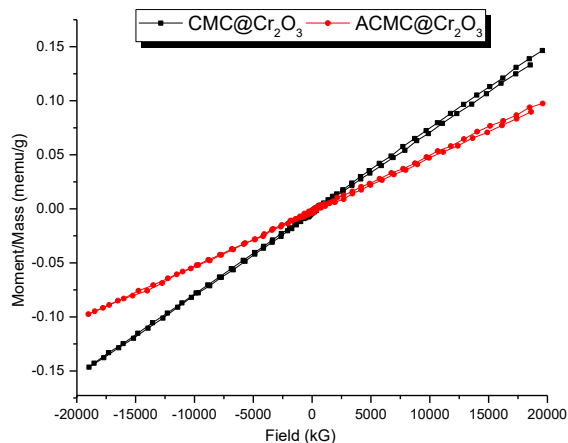


Figure 9: VSM of fabricated  $\text{CMC}@Cr_2O_3$  and  $\text{ACMC}@Cr_2O_3$ .

Table 4: Thermoanalytical parameters of the CMC, ACMC and their analogues Cr<sub>2</sub>O<sub>3</sub> nanocomposites

Sample	TG parameters						Kinetic and thermodynamic parameters						
	Degradation step	Temp. range, °C	On-set, °C	Off-set, °C	Peak maximum, °C	Δm, %	R <sub>700°</sub> (%)	E <sub>a</sub> , kJ/mol	A, 1/s	ΔH <sub>a</sub> , kJ/mol	ΔS <sub>a</sub> , J/mol.K	ΔG <sub>a</sub> , kJ/mol	R <sup>2</sup>
CMC	1 <sup>st</sup>	33-112	298	353	331	1.39	0.0	231.00	1.4X10 <sup>19</sup>	225.98	115.76	156.06	0.99
	2 <sup>nd</sup>	259-377				98.73							
ACMC	1 <sup>st</sup>	33-138	35	118	72	1.87	24.75	184.06	3.59X10 <sup>14</sup>	178.86	27.57	161.60	0.98
	2 <sup>nd</sup>	215-396	320	373	353	73.03							
CMC@Cr <sub>2</sub> O <sub>3</sub>	1 <sup>st</sup>	44-158	47	138	84	2.74	65.61	78.20	5.11X10 <sup>5</sup>	73.30	-141.33	156.54	0.97
	2 <sup>nd</sup>	212-365	274	353	316	20.29							
ACMC@Cr <sub>2</sub> O <sub>3</sub>	1 <sup>st</sup>	35-164	36	132	71	3.35	72.34	92.45	110.05X10 <sup>5</sup>	87.52	-115.838	156.10	0.99
	2 <sup>nd</sup>	210-365	238	349	319	17.52							

The onset temperature of the decompositions is the temperature at which the DTG curve begins to deviate from its baseline.  
 The offset temperature at which decomposition occurs, indicated by the point at which the DTG curve returns to its baseline.  
 The peak maximum temperature, also known as the temperature at which the weight loss rate is highest, is determined by finding the place where tangents intersect at the peak of the DTG curve.  
 The weight loss throughout the decomposition phase (Δm) corresponds to the mass reduction occurring between the onset temperature and the offset temperature on the TG curve.

Table 5: The magnetic parameters from VSM analysis

Parameter	CMC@Cr <sub>2</sub> O <sub>3</sub>	ACMC@Cr <sub>2</sub> O <sub>3</sub>
Saturation Magnetization (Ms)	146.45X10 <sup>-3</sup> emu/g	97.48X10 <sup>-3</sup> emu/g
Remanent Magnetization (Mr)	-2.74X10 <sup>-3</sup> emu/g	-1.42X10 <sup>-3</sup> emu/g
Coercivity (Hci)	564.2 G	349.97 G
S Parameter	4.77X10 <sup>-3</sup>	1.27X10 <sup>-2</sup>
TA (Energy Parameter)	102.06 erg/g	72.33 erg/g
Magnetic Behavior	Paramagnetic	Paramagnetic

#### 4. Conclusion

Collectively, the results show that the characteristics of cellulose-based matrices are drastically changed when Cr<sub>2</sub>O<sub>3</sub> is integrated into them. According to XRD results, forming CMC@Cr<sub>2</sub>O<sub>3</sub> and ACMC@Cr<sub>2</sub>O<sub>3</sub> results in smaller average crystallite sizes. This suggests that bonding with Cr<sub>2</sub>O<sub>3</sub> promotes a change in the main cellulose structure. In ACMC@Cr<sub>2</sub>O<sub>3</sub>, the band gap has been red-shifted from 3.66 eV in CMC@Cr<sub>2</sub>O<sub>3</sub> to 3.36 eV, according to DRS results. This is most likely due to impurity levels formed within the band gap, likely caused by vacancies and defects introduced by Na<sup>+</sup>.

Despite sharing comparable CMC particle morphologies, scanning electron microscopy (SEM) imaging shows that the two composites' surface coatings differ. CMC@Cr<sub>2</sub>O<sub>3</sub> exhibits discrete clusters of Cr<sub>2</sub>O<sub>3</sub> nanoparticles, whereas ACMC@Cr<sub>2</sub>O<sub>3</sub> forms a crust covering the fibers' surfaces. Chromium, carbon, and oxygen are evenly distributed throughout the matrix, according to EDX evaluation.

TGA shows that the Cr<sub>2</sub>O<sub>3</sub> coating improves thermal stability by lowering the activation energy and pre-exponential factors for pyrolysis. This effect is much more noticeable in the ACMC@Cr<sub>2</sub>O<sub>3</sub> that has been activated with alkali. In contrast to CMC@Cr<sub>2</sub>O<sub>3</sub>, the nucleation and distribution of Cr<sub>2</sub>O<sub>3</sub> particles are affected by the changes in the ionic environment and cellulose biopolymer conformation brought about by the sodium inclusion in ACMC.

The activation process significantly influenced the nucleation and dispersion of Cr<sub>2</sub>O<sub>3</sub> nanoparticles, altering cellulose's ionic environment and biopolymer conformation. These changes reduced saturation magnetization, remanent magnetization, and coercivity in ACMC@Cr<sub>2</sub>O<sub>3</sub>. Interestingly, the higher S value observed in ACMC@Cr<sub>2</sub>O<sub>3</sub> may reflect changes in the magnetic domain structure and switching dynamics. While both composites retained their paramagnetic nature, sodium appeared to induce a finer, more heterogeneous microstructure with reduced magnetic interactions, further highlighting the role of activation in tailoring composite properties.

#### 5. Conflict of interest

There is no conflict of interest.

#### 6. Acknowledgement

The authors extend their heartfelt gratitude to Al-Azhar University and the National Research Centre for their invaluable support in supplying the chemical resources, instruments, and state-of-the-art facilities that were crucial to the success of this research.

#### 7. References

- [1] Rishch RS, Vazvani MG, Hassanisaadi M, Thakur VK. Agricultural wastes: A practical and potential source for the isolation and preparation of cellulose and application in agriculture and different industries. *Ind Crops Prod* 2024;208:117904. <https://doi.org/10.1016/j.indcrop.2023.117904>.
- [2] Chia MR, Phang SW, Mohd Razali NS, Ahmad I. Approach towards sustainable circular economy: waste biorefinery for the production of cellulose nanocrystals. *Cellulose* 2024;31:3377–420. <https://doi.org/10.1007/s10570-024-05825-9>.
- [3] Makam RMM, Wan Omar WNN, Ahmad DA bin J@., Nor NUM, Shamjuddin A, Amin NAS. The potential of carboxylmethyl cellulose from empty fruit bunch as versatile material in food coating: A review. *Carbohydr Polym* 2024;338:122194. <https://doi.org/10.1016/j.carbpol.2024.122194>.
- [4] Plianwong S, Sirirak T. Cellulose nanocrystals from marine algae *Cladophora glomerata* by using microwave-assisted extraction. *Int J Biol Macromol* 2024;260:129422. <https://doi.org/10.1016/j.ijbiomac.2024.129422>.
- [5] Poudel J, Bhattarai S, Tara A, Rahman MF, Nath N, Tanti B. Recent progress in microcrystalline cellulose for solar cell applications: a comprehensive review. *J Opt* 2025:1–15.
- [6] Techawinyutham L, Sundaram RS, Suyambulingam I, Mo-On S, Srisuk R, Divakaran D, Rangappa SM, Siengchin S. Rice husk biowaste derived microcrystalline cellulose reinforced sustainable green composites: A comprehensive characterization for lightweight applications. *Int J Biol Macromol* 2025;299:140153.

- [7] Poudel J, Bhattarai S, Nath N, Tanti B. An Exclusive Review of Microcrystalline Cellulose: Structure and Applications, and Limitations. *Mater Today Commun* 2025;112247.
- [8] El-Gendy A, El-Sakhawy M, Adel AM, Al-Shemy MT. Effect of Microcrystalline Cellulose as a Filler and/or Filler Retention Aid on the Mechanical Properties of Bagasse Paper Sheets. *Cellul Chem Technol* 2020;54:993–1000. <https://doi.org/10.35812/CelluloseChemTechnol.2020.54.96>.
- [9] Wang W, Wang F, Zhang C, Wang Z, Tang J, Zeng X, Wan X. Robust, Reprocessable, and Reconfigurable Cellulose-Based Multiple Shape Memory Polymer Enabled by Dynamic Metal-Ligand Bonds. *ACS Appl Mater Interfaces* 2020;12:25233–42. <https://doi.org/10.1021/acsami.9b13316>.
- [10] Yue C, Ding C, Yang N, Luo Y, Su J, Cao L, Cheng B. Strong and tough collagen/cellulose nanofibril composite films via the synergistic effect of hydrogen and metal–ligand bonds. *Eur Polym J* 2022;180:111628. <https://doi.org/10.1016/j.eurpolymj.2022.111628>.
- [11] Al-Shemy M, El-Shafie A, Alaneny A, Adel A. Facile In-Situ Synthesis of Nanocrystalline Celluloses-Silver Bio-nanocomposite for Chitosan Based Active Packaging. *Egypt J Chem* 2023;66:335–52. <https://doi.org/10.21608/ejchem.2022.149568.6465>.
- [12] Ibrahim AA, Adel AM, El-Wahab ZHA, Al-Shemy MT. Utilization of carboxymethyl cellulose based on bean hulls as chelating agent. Synthesis, characterization and biological activity. *Carbohydr Polym* 2011;83:94–115. <https://doi.org/10.1016/j.carbpol.2010.07.026>.
- [13] Al-Shemy MT, Nasralla N, Turkey G, Wang Q, Yang Y, Kamel S. Preparation, characterization and performance evaluation of methylcellulose/CuS@rGO/PANI membrane for energy storage application. *Diam Relat Mater* 2025;152:111908. <https://doi.org/10.1016/j.diamond.2024.111908>.
- [14] El-Sayed NS, El-Sakhawy M, Hesemann P, Brun N, Kamel S. Rational design of novel water-soluble ampholytic cellulose derivatives. *Int J Biol Macromol* 2018;114:363–72. <https://doi.org/10.1016/j.ijbiomac.2018.03.147>.
- [15] Alamdari NE, Aksoy B, Babu RJ, Jiang Z. Microcrystalline cellulose from soybean hull as an excipient in solid dosage forms: Preparation, powder characterization, and tableting properties. *Int J Biol Macromol* 2024;270:132298. <https://doi.org/10.1016/j.ijbiomac.2024.132298>.
- [16] Mishra S. New Excipient For Oral Drug Delivery: CNC Derived From Sugarcane Bagasse-Derived Microcrystalline Cellulose. *ACS Omega* 2024;9:19353–62. <https://doi.org/10.1021/acsomega.4c00497>.
- [17] Zuo HF, Guo YR, Li SJ, Pan QJ. Application of microcrystalline cellulose to fabricate ZnO with enhanced photocatalytic activity. *J Alloys Compd* 2014;617:823–7. <https://doi.org/10.1016/j.jallcom.2014.08.071>.
- [18] Wibowo CH, Ariawan D, Surojo E, Sunardi S. Microcrystalline Cellulose as Composite Reinforcement: Assessment and Future Prospects. *Mater. Sci. Forum*, vol. 1122, 2024, p. 65–80.
- [19] Liang S, Zhang H, Luo M, Luo K, Li P, Xu H, Zhang Y. Colour performance investigation of a Cr<sub>2</sub>O<sub>3</sub> green pigment prepared via the thermal decomposition of CrOOH. *Ceram Int* 2014;40:4367–73.
- [20] Sangeetha S, Basha R, Sreeram KJ, Sangilimuthu SN, Nair BU. Functional pigments from chromium (III) oxide nanoparticles. *Dye Pigment* 2012;94:548–52.
- [21] Gibot P, Vidal L. Original synthesis of chromium (III) oxide nanoparticles. *J Eur Ceram Soc* 2010;30:911–5.
- [22] Ali SQ, Aziz WJ, Kadhim DA, Abid MA, Sabry RS. Corn plant leaf extract inhibits microbial growth with the photocatalytic activities of MB, MO, and RdB dye-mediated nano-Cr<sub>2</sub>O<sub>3</sub>. *Nano-Structures and Nano-Objects* 2024;39:101257. <https://doi.org/10.1016/j.nanoso.2024.101257>.
- [23] Dubey V, Parikh KD, Jadav RJ, Vyas DH, Avinash B, Ravikumar CR, Kumar AN, Rao HS, Kumar D, Ghotekar S. Eco-Friendly Fabrication of Cr<sub>2</sub>V<sub>4</sub>O<sub>13</sub> Nanoparticles: A Promising Material for Photocatalysis, Electrochemical Sensing, and Supercapacitor Applications. *J Clust Sci* 2025;36:1–23.
- [24] Muzammal S, Ali S, Ahmad A, Habila MA. Eco-friendly Cr<sub>2</sub>O<sub>3</sub> nanoparticles from *Opuntia dillenii* for visible-light photocatalysis and antimicrobial defense against waterborne pathogens. *Ceram Int* 2025;51:5159–67.
- [25] Kuranov D, Konstantinova E, Grebenkina A, Sagitova A, Platonov V, Polomoshnov S, Rummyantseva M, Krivetskiy V. Cr-Doped Nanocrystalline TiO<sub>2</sub>-Cr<sub>2</sub>O<sub>3</sub> Nanocomposites with pp Heterojunction as a Stable Gas-Sensitive Material. *Int J Mol Sci* 2025;26:499.
- [26] Hossain R, Appleby A. Cr<sup>3+</sup>-Doped Anatase-Phase TiO<sub>2</sub> Nanocrystals with (101) and (004) Dominant Facets: Synthesis and Characterization. *Catalysts* 2025;15:33.
- [27] Terea H, Rebiai A, Selloum D, Tedjani ML. Cellulose/ZnO nanoparticles (CNC/ZnO NPs): synthesis, characterization, and evaluation of their antibacterial and antifungal activities. *Cellulose* 2024;31:5027–42. <https://doi.org/10.1007/s10570-024-05912-x>.
- [28] Liang Y, Liu X, Wang L, Sun J. The fabrication of microcrystalline cellulose-nanoZnO hybrid composites and their application in rubber compounds. *Carbohydr Polym* 2017;169:324–31. <https://doi.org/10.1016/j.carbpol.2017.04.022>.
- [29] Fu B, Xie F. Facile in situ synthesis of cellulose microcrystalline-manganese dioxide nanocomposite for effective removal of Pb(II) and Cd(II) from water. *Environ Sci Pollut Res* 2020;27:5108–21. <https://doi.org/10.1007/s11356-019-07159-7>.
- [30] Kumar B, Reddy MS, Dwivedi KD, Dahiya A, Babu JN, Chowhan LR. Synthesis of in situ immobilized iron oxide nanoparticles (Fe<sub>3</sub>O<sub>4</sub>) on microcrystalline cellulose: Ecofriendly and recyclable catalyst for Michael addition. *Appl Organomet Chem* 2022;36:e6455. <https://doi.org/10.1002/aoc.6455>.
- [31] El Shall F, Al-Shemy M. In-Situ Fabrication of Polyurethane Acrylate/Zinc Oxide NPs Frameworks as dual-function Water-borne Binders for Blend Fabrics Printing. *Egypt J Chem* 2024;67:423–35. <https://doi.org/10.21608/EJCHEM.2023.212517.8003>.
- [32] Al-Shemy MT, Gamoń F, Al-Sayed A, Hellal MS, Ziemińska-Buczyńska A, Hassan GK. Silver nanoparticles incorporated with superior silica nanoparticles-based rice straw to maximize biogas production from anaerobic digestion of landfill leachate. *J Environ Manage* 2024;365:121715. <https://doi.org/10.1016/j.jenvman.2024.121715>.

- [33] Adel AM, Abd El-Wahab ZH, Ibrahim AA, Al-Shemy MT. Characterization of microcrystalline cellulose prepared from lignocellulosic materials. Part II: Physicochemical properties. *Carbohydr Polym* 2011;83:676–87. <https://doi.org/10.1016/j.carbpol.2010.08.039>.
- [34] Heinze T, El Seoud OA, Koschella A. Cellulose Activation and Dissolution. 2018. [https://doi.org/10.1007/978-3-319-73168-1\\_3](https://doi.org/10.1007/978-3-319-73168-1_3).
- [35] Varma RSS, Vikram KA, Chekuri RBR, Kotteda TK. Comprehensive characterization of microcrystalline cellulose from *Myriophyllum verticillatum* algae: From biomass to biomaterial for polymer composite applications. *Int J Biol Macromol* 2025;309:142659. <https://doi.org/10.1016/j.ijbiomac.2025.142659>.
- [36] Baruah J, Deka RC, Kalita E. Greener production of microcrystalline cellulose (MCC) from *Saccharum spontaneum* (Kans grass): Statistical optimization. *Int J Biol Macromol* 2020;154:672–82. <https://doi.org/10.1016/j.ijbiomac.2020.03.158>.
- [37] Palaniappan M, Palanisamy S, Khan R, H.Alrashedi N, Tadepalli S, Murugesan T mani, Santulli C. Synthesis and suitability characterization of microcrystalline cellulose from *Citrus x sinensis* sweet orange peel fruit waste-based biomass for polymer composite applications. *J Polym Res* 2024;31:105. <https://doi.org/10.1007/s10965-024-03946-0>.
- [38] Sunesh NP, Indran S, Divya D, Suchart S. Isolation and characterization of novel agrowaste-based cellulosic micro fillers from *Borassus flabellifer* flower for polymer composite reinforcement. *Polym Compos* 2022;43:6476–88. <https://doi.org/10.1002/pc.26960>.
- [39] Divakaran D, Suyambulingam I, Sanjay MR, Raghunathan V, Ayyappan V, Siengchin S. Isolation and characterization of microcrystalline cellulose from an agro-waste tamarind (*Tamarindus indica*) seeds and its suitability investigation for biofilm formulation. *Int J Biol Macromol* 2024;254:127687. <https://doi.org/10.1016/j.ijbiomac.2023.127687>.
- [40] Katakajwala R, Mohan SV. Microcrystalline cellulose production from sugarcane bagasse: Sustainable process development and life cycle assessment. *J Clean Prod* 2020;249:119342. <https://doi.org/10.1016/j.jclepro.2019.119342>.
- [41] Boopasiri S, Thaptong P, Sae-Oui P, Siritwong C. Fabrication of zinc oxide-coated microcrystalline cellulose and its application in truck tire tread compounds. *J Appl Polym Sci* 2022;139. <https://doi.org/10.1002/app.52701>.
- [42] Al Lafi AG, Khuder A. Removal of Cr (VI) from aqueous solutions by activated carbon and its composite with P2W17O61: A spectroscopic study to reveal adsorption mechanism. *Heliyon* 2025;11.
- [43] Al-Shemy MT, El-Demerdash AS, Marzec A, Dawwam GE. Biocontrol of virulent *Listeria monocytogenes* using green carboxylated cellulose nanocrystals–silver nano-biohybrids. *Int J Biol Macromol* 2025;290:139012. <https://doi.org/10.1016/j.ijbiomac.2024.139012>.
- [44] El-Sabour MA, Mohamed AL, El-Meligy MG, Al-Shemy MT. Characterization of recycled waste papers treated with starch/organophosphorus-silane biocomposite flame retardant. *Nord Pulp Pap Res J* 2021;36:108–24. <https://doi.org/10.1515/npprj-2020-0075>.
- [45] Zayed EA, Alian NA, Gomaa EH, Shaker NO. Vision for a better future with synthesized polyurethane amide as an enhancer for cotton fabric properties. *Int J Theor Appl Res* 2025;3:490–504. <https://doi.org/10.21608/ijtar.2024.314068.1083>.
- [46] Adel AM, El-Shafei A, Ibrahim A, Al-Shemy M. Extraction of oxidized nanocellulose from date palm (*Phoenix Dactylifera* L.) sheath fibers: Influence of CI and CII polymorphs on the properties of chitosan/bionanocomposite films. *Ind Crops Prod* 2018;124:155–65. <https://doi.org/10.1016/j.indcrop.2018.07.073>.
- [47] Adel AM, Al-Shemy MT, Diab MA, El-Sakhawy M, Toro RG, Montanari R, de Caro T, Caschera D. Fabrication of packaging paper sheets decorated with alginate/oxidized nanocellulose-silver nanoparticles bio-nanocomposite. *Int J Biol Macromol* 2021;181:612–20. <https://doi.org/10.1016/j.ijbiomac.2021.03.182>.
- [48] Hidayat M, Aqilah NA, Winata A. Pretreatment of Oil Palm Empty Fruit Bunch using Caustic Soda Solution for Lignin Isolation. *J Appl Sci Eng* 2022;25:1025–30. [https://doi.org/10.6180/jase.202212\\_25\(6\).0013](https://doi.org/10.6180/jase.202212_25(6).0013).
- [49] Varma R, Vasudevan S. Synthesis and Characterization of Cellulose and Cellulose Nanocrystals From Dead Seagrass – Towards the Wealth From Waste Concept. *Cellul Chem Technol* 2022;56:39–47. <https://doi.org/10.35812/CelluloseChemTechnol.2022.56.03>.
- [50] El-Shall FN, Al-Shemy MT, Hagag KH, Adel AM. Fabrication of microwave silicified oxidized cellulose nanocrystals (SOCN) from Agro waste for sustainable multifunctional wool fabric coloration. *J Clean Prod* 2023;386:135800. <https://doi.org/10.1016/j.jclepro.2022.135800>.
- [51] Hady AK, Owda ME, Abouzeid RE, Shehata HA, Elzaref AS, Elfeky AS. Harnessing the potential of modified cellulosic pumpkin seed hulls as affordable biosorbents for cationic dye removal from aqueous solutions: adsorption kinetics and isotherm studies. *Biomass Convers Biorefinery* 2025;15:759–73. <https://doi.org/10.1007/s13399-023-05146-0>.
- [52] Deepak HN, Choudhari KS, Shivashankar SA, Santhosh C, Kulkarni SD. Facile microwave-assisted synthesis of Cr<sub>2</sub>O<sub>3</sub> nanoparticles with high near-infrared reflection for roof-top cooling applications. *J Alloys Compd* 2019;785:747–53.
- [53] Xie D, Luo Q, Zhou S, Zu M, Cheng H. One-step preparation of Cr<sub>2</sub>O<sub>3</sub> -based inks with long-term dispersion stability for inkjet applications. *Nanoscale Adv* 2021;3:6048–55. <https://doi.org/10.1039/d1na00244a>.
- [54] Sultan FA, El-Salamony RA, Said SA, Abdu KS. Preparation and Characterization of Cobalt and Zinc Oxide Nanoparticles using Green Synthesis method for technological development. *Al-Azhar Bull Sci* 2025;36:28–37. <https://doi.org/10.21608/2636-3305.1694>.
- [55] El-Sayed NS, Awad H, El-Sayed GM, Nagieb ZA, Kamel S. Synthesis and characterization of biocompatible hydrogel based on hydroxyethyl cellulose-g-poly(hydroxyethyl methacrylate). *Polym Bull* 2020;77:6333–47. <https://doi.org/10.1007/s00289-019-02962-1>.
- [56] Khamis M, Gouda GA, Nagiub AM. Green Synthesis Of Zinc Oxide Nanoparticles: Characterization, Organic Dye Degradation And Evaluation Of Their Antibacterial Activity. *Al-Azhar Bull Sci* 2023;34:84–101. <https://doi.org/10.58675/2636-3305.1650>.

- [57] Zhang H, Wang X, Wang J, Chen Q, Huang H, Huang L, Cao S, Ma X. UV–visible diffuse reflectance spectroscopy used in analysis of lignocellulosic biomass material. *Wood Sci Technol* 2020;54:837–46. <https://doi.org/10.1007/s00226-020-01199-w>.
- [58] Siva KV, Bhowmik RN. Structural, magnetic and magneto-electric properties of Cr doped  $\alpha$ -Fe<sub>2</sub>O<sub>3</sub>. *AIP Conf. Proc.*, vol. 2115, AIP Publishing; 2019.
- [59] Bhardwaj P, Singh J, Kumar R, Kumar R, Verma V. Structural, optical and magnetic characterization of Ni<sup>2+</sup> ions doped chromium oxide (Cr<sub>2</sub>O<sub>3</sub>) nanoparticles. *Solid State Sci* 2021;115:106581. <https://doi.org/10.1016/j.solidstatesciences.2021.106581>.
- [60] Srinivasan P, Sahadevan J, Sankaran EM, Kim I, Arangarasan V, Paramasivam S. Investigating the impact of sodium (Na) dopant on the structural, morphological, optical, and magnetic properties of LaPrSrMnO<sub>3</sub> perovskite nanoflakes 2024;238:1943–57. <https://doi.org/doi:10.1515/zpch-2023-0490>.
- [61] Khanagwal J, Khatkar SP, Dhankhar P, Bala M, Kumar R, Boora P, Taxak VB. Synthesis and photoluminescence analysis of europium(III) complexes with pyrazole acid and nitrogen containing auxiliary ligands. *Spectrosc Lett* 2020;53:625–47. <https://doi.org/10.1080/00387010.2020.1817093>.
- [62] El-Sayed NS, Moussa MA, Kamel S, Turkey G. Development of electrical conducting nanocomposite based on carboxymethyl cellulose hydrogel/silver nanoparticles@polypyrrole. *Synth Met* 2019;250:104–14. <https://doi.org/10.1016/j.synthmet.2019.03.010>.
- [63] Hasanin MS, Al-Shemy MT, Eisa WH, Kamel S. Green biodegradable ultraviolet shielding membrane-based cellulose and lignin-doped photoactive core-shell nano bimetallic. *J Environ Chem Eng* 2025;13. <https://doi.org/10.1016/j.jece.2024.115176>.
- [64] Aziz AA, Nassar HF, Al-Shemy MT, Mohamed OA. Boosting the mechanical performance and fire resistivity of white ordinary portland cement pastes via biogenic mesoporous silica nanoparticles. *Sci Rep* 2025;15:2909. <https://doi.org/10.1038/s41598-025-86798-y>.
- [65] EL-Sayed NS, Dacrory S, El-Sakhawy M, Hassan EB, Kamel S. Fabrication of nanocomposite based on oxidized biochar and oxidized cellulose nanofibers and its potential cd(II) adsorption. *Adsorption* 2025;31:56. <https://doi.org/10.1007/s10450-025-00610-x>.
- [66] Barakat A, Ehagali GAM, Kamoun EA, Abusaif MS, Owda ME, Ghazy MB, Ammar YA. A novel chitosan-Schiff bases bearing a new quinoxaline moiety as an approach for potent antimicrobial agent: Synthesis, characterization and in vitro assessments. *Carbohydr Polym* 2025;352:123205. <https://doi.org/10.1016/j.carbpol.2024.123205>.
- [67] Ali IO, Nassar HS, El-Nasser KS, Bougarech A, Abid M, Elhenawy AA. Synthesis and characterization of Mn<sup>II</sup> and Co<sup>II</sup> complexes with poly (vinyl alcohol-nicotinic acid) for photocatalytic degradation of Indigo carmine dye. *Inorg Chem Commun* 2021;124:108360. <https://doi.org/10.1016/j.inoche.2020.108360>
- [68] Jiang J, Li J, Hu J, Fan D. Effect of nitrogen phosphorus flame retardants on thermal degradation of wood. *Constr Build Mater* 2010;24:2633–7. <https://doi.org/10.1016/j.conbuildmat.2010.04.064>.
- [69] Dave A, Gupta GK, Mondal MK. Study on thermal degradation characteristics, kinetics, thermodynamic, and reaction mechanism analysis of Arachis hypogaea shell pyrolysis for its bioenergy potential. *Biomass Convers Biorefinery* 2023;13:9289–304. <https://doi.org/10.1007/s13399-021-01749-7>.
- [70] Niu S, Yu H, Zhao S, Zhang X, Li X, Han K, Lu C, Wang Y. Apparent kinetic and thermodynamic calculation for thermal degradation of stearic acid and its esterification derivants through thermogravimetric analysis. *Renew Energy* 2019;133:373–81. <https://doi.org/10.1016/j.renene.2018.10.045>.
- [71] Abu-Elsaad NI, Nawara AS. Effect of Cu substitution on magnetic and photocatalytic properties of Mn–ZnFe<sub>2</sub>O<sub>4</sub> nanoparticles. *J Mater Sci* 2024;59:4167–85. <https://doi.org/10.1007/s10853-024-09486-8>.